

Neutron Interaction Properties of Structural Materials for Multi-Grid Neutron Detectors

A. Backis^a, C.-C. Lai^a, M. Aouane^a, P.P. Deen^a, K.G. Fissum^a, J.R.M. Annand^b, K. Livingston^b, D. Raspino^c

^aEuropean Spallation Source ERIC, SE-221 00 Lund, Sweden

^bSchool of Physics and Astronomy, University of Glasgow G12 8QQ, Scotland, UK

^cISIS Facility, Rutherford Appleton Laboratory, Harwell Campus, Oxfordshire OX11 0QX, UK

Abstract

The T-REX neutron time-of-flight spectrometer at the European Spallation Source will use Multi-Grid Technology, which relies on thin B₄C coatings on the Al blades of the grids to detect scattered thermal neutrons. Following a Monte Carlo study of internal shielding to suppress neutron multiple scattering in T-REX, the neutron transmission and scattering properties of 12 shielding-material samples have been measured at the ISIS spallation neutron source. Neutron transmission was measured on the EMMA beam line at wavelengths 0.5–4.7 Å, using a 2D-position-sensitive, neutron GEM detector, while neutron scattering was measured for 6 of the samples at the Merlin spectrometer, at wavelengths 0.72, 1.28, 1.85 and 2.41 Å. The present tests show that a B₄C/Al composite material, plated with Ni to stop intrinsic alpha background, is an effective neutron absorber, suitable for incorporation in the Multi-Grid structures which detect the neutrons in inelastic neutron spectrometers.

1. Introduction

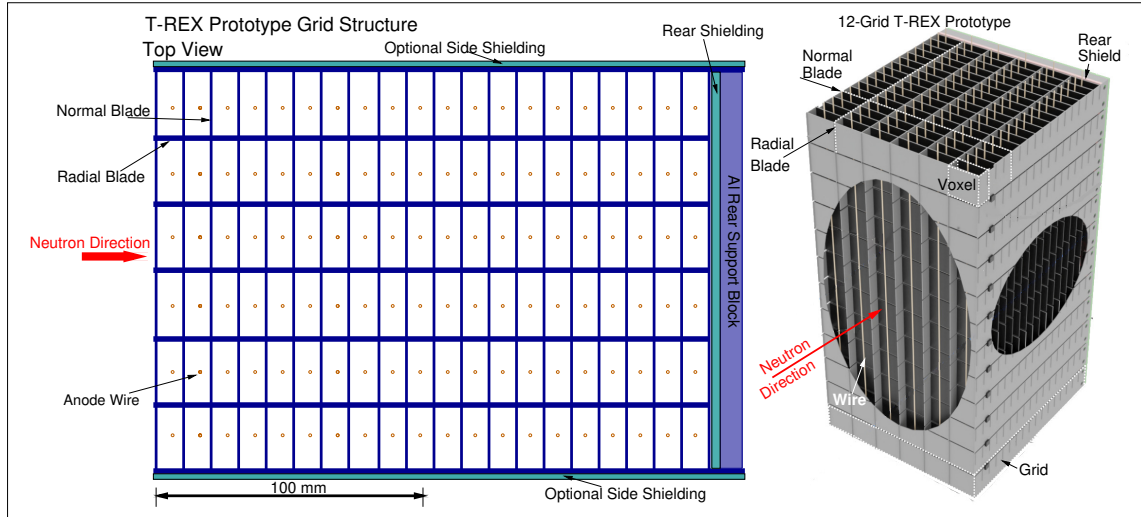


Figure 1: Left: prototype T-REX grid. Each voxel has an internal dimension of 23.5 mm (x) by 24.0 mm (y) by 9.5 mm (z). Right: 3D view of a 12-grid T-REX prototype, with outer sections cut away to reveal the internal structure.

*Corresponding Author

Email address: john.annand@glasgow.ac.uk (J.R.M. Annand)

Multi-Grid (MG) technology for detection of sub-eV neutrons, originally developed at ILL [1], will be used in the T-REX bispectral chopper spectrometer which is under construction at the European Spallation Source (ESS) [2]. The Multi-Grids are stacks of grids, each a rectangular lattice of normal and radial Al blades (Fig.1). The grids form the cathodes of a voxelised proportional counter (VPC), with wires strung through the centres of each grid voxel providing the anodes. The normal blades are coated with ^{10}B -enriched B_4C , and neutron capture in the B_4C film produces ^4He and ^7Li ions, one of which escapes into the VPC gas (e.g. Ar-CO₂) giving a detectable signal. Al is the main structural material for both the grids, their support mechanics and the gas containment vessels, as its neutron absorption cross section is relatively low. Nevertheless neutrons can scatter internally in the Al and other nearby materials before they eventually convert and this distorts the time-of-flight (TOF) and angle-of-detection measurement, thereby distorting the energy and momentum-transfer measurement by the spectrometer.

Internal neutron scattering can be suppressed by installation of internal shielding [3, 4, 5], at the sides and rear of the MG and on the radial blades of the grids. Monte Carlo simulations of neutron scattering from Vanadium into T-REX [6] indicate that internal shielding materials based on B_4C can result in a major reduction in internal scattering within the spectrometer. Scintered B_4C sheet would be a possibility for side and rear shields, but structurally this is a difficult material and it is unsuitable for radial blades, which must be electrically conductive. A number of materials containing B_4C are available and their shielding effectiveness has been investigated using the Geant4 [7] model of T-REX. Subsequently neutron transmission and scattering properties of good candidate shielding materials were measured at the EMMA [8] and MERLIN [9] beam lines of the neutron-spallation facility ISIS and compared to Geant4 simulations of these test measurements.

2. Neutron Transmission Tests at EMMA

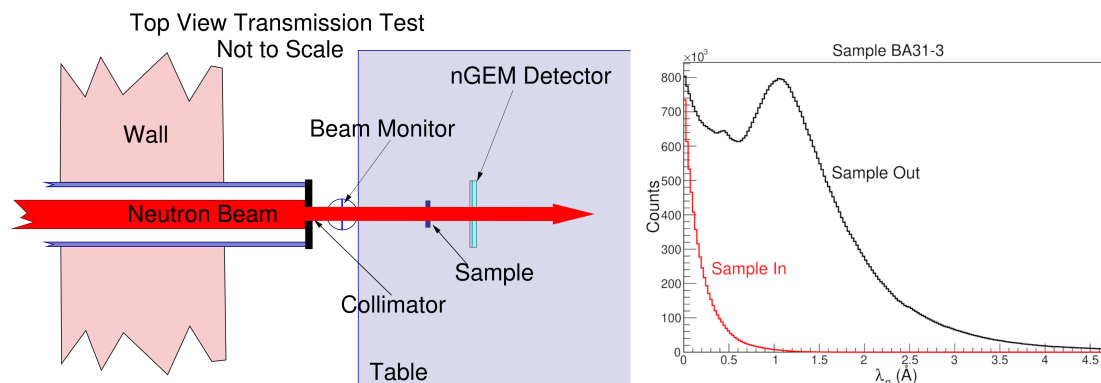


Figure 2: Left: schematic diagram of the EMMA neutron transmission test. Right: comparison of sample in/out wavelength spectra derived from TOF at the nGEM detector. The sample was BA31-3 (see Table 1).

Measurements of neutron transmission through samples of shielding material were performed on the EMMA beam line, with the Fermi chopper powered down to produce a white neutron beam. A schematic of the experimental setup is shown in Fig. 2 (left plot), while the neutron wavelength spectrum is displayed in Fig. 2 (right plot, sample out). The samples are listed in Table 1.

The neutron beam was collimated by movable B_4C jaws, set to produce a rectangular aperture of $25 \times 50 \text{ mm}^2$. It then passed through a low efficiency beam monitor (BM), the sample under study, and a 2D, position-sensitive neutron gas electron multiplier (nGEM) detector [10]. The BM was a 0.25 mm sheet of GS1 scintillating glass, with a neutron efficiency of $\sim 0.5\%$ at a wavelength of ~ 1 Å. The nGEM was a $10 \times 10 \text{ mm}^2$ GEM chamber read out by 128 x and 128 y strips (0.8 mm pitch), with a thin layer of ^{10}B deposited on the cathode to convert neutrons to detectable ions. The intersections between x and y strips define 16384 pixels. TOF was recorded for the nGEM strips and BM. Samples were rectangular sheets of the material under study inserted into the neutron beam, downstream of the BM and perpendicular to the beam direction.

Name	Substrate	Coating	B ₄ C(%)	¹⁰ B(%)	Slope ±5%	G4	<i>k</i>
Al	HP Al 0.5 mm	–	–	–	0.00		0.00
Al-5	HP Al 0.5 mm	Sputtered B ₄ C 5 μm	100	97	0.18	0.23	0.23
Dr-10	Al 0.5 mm	DripB ₄ C/Epoxy 10 μm	73.8	92	0.47	0.25	0.25
Dr-20	Al 0.5 mm	DripB ₄ C/Epoxy 20 μm	73.8	92	1.04	0.50	0.50
Sp1.4	Al 1 mm	SprayedB ₄ C/Al 300 μm	52	19.9	0.56	1.41	1.39
Sp1.6	Al 1 mm	SprayedB ₄ C/Al 300 μm	52	19.9	1.19	1.41	1.39
BA31-1	Al/B ₄ C 1 mm	–	31	19.9	1.54	1.52	1.51
NiBA31-1	Al/B ₄ C 0.95 mm	Plated Ni 25 μm	31	19.9	1.43	1.45	1.43
BA31-2	Al/B ₄ C 2 mm	–	31	19.9	3.06	3.03	3.03
BA31-3	Al/B ₄ C 3 mm	–	31	19.9	4.55	4.59	4.54
BA25-3	Al/B ₄ C 3 mm	–	25	19.9	3.54	3.67	3.68
BA25-8	Al/B ₄ C 8 mm	–	25	19.9	9.54	9.93	9.82

Table 1: Shielding candidate materials. Column ‘Substrate’ is the substrate material of the sample where HP stands for High Purity. Coating (if applied) is the coating applied to the substrate. ‘B₄C(%)’ is the content by weight of B₄C in the substrate or coating and ‘¹⁰B(%)’ is the ¹⁰B content (19.9% in natural B). Slope is the exponential decay constant fitted to the averaged R_{io} transmission measurement displayed in Fig. 3. G4 is the decay constant fitted to the Geant4 calculation and $k = 2133N_{10}t$ is a hand calculation (see text) of the decay constant, based on a ¹⁰B capture cross section [13] $\sigma = 2133\lambda_n$ b.

Runs were made with sample in and sample out, for equal accumulations of proton charge on the spallation target. Counts in the nGEM pixels were normalised to equal neutron counts in the beam monitor and the ratio (R_{io}) of sample-in/sample-out counts gives a measure of the neutron transmission probability through the sample. Fig. 3 displays R_{io} , averaged over the area of the sample, as a function of neutron wavelength λ_n . Those nGEM pixels at the edges of the sample shadow and those pixels showing the slots in the sample (see Fig. 4) were omitted from the averaging procedure. If neutron capture on ¹⁰B is the dominant determinant of the transmission and the capture cross section depends linearly on wavelength ($\sigma = 2133\lambda_n$ b [13]), then $R_{io} = \exp(-k\lambda_n)$. Here $k = 2133N_{10}t$, where N_{10} is the density of ¹⁰B atoms in the sample and t is the sample thickness. Thus on a logarithmic scale R_{io} should appear linear in λ_n . In the higher k samples there is a significant departure from linearity at longer wavelengths.

The EMMA beam line and end station are not evacuated so that there is significant air scattering of neutrons and in addition, the region around the collimator is weakly shielded. Thus the neutron beam has a substantial halo which produced background counts in the nGEM, irrespective of any sample in the path of the beam. At longer wavelengths, with the more opaque samples, the background becomes significant with respect to the sample-in counts and this distorts the ratio. The 480 keV gamma produced in 94% of ¹⁰B capture events can in principle also add to background. As k increases the number of neutrons reaching the nGEM decreases, but the number of capture gammas increases. However the Geant4 simulation, which has a simplified model of the nGEM but does not include beam halo effects, predicts that the gamma contribution to background will be very small.

The measured and Geant4 simulated transmission curves in Fig. 3 were fitted with exponentials and the resulting slope constants are given in Table 1. Longer wavelengths, where the measured ratio departs significantly from exponential, were excluded from the fits and the uncertainty in the fitted value is $\sim \pm 5\%$. The Geant4 values are consistent with the hand calculations of k described above.

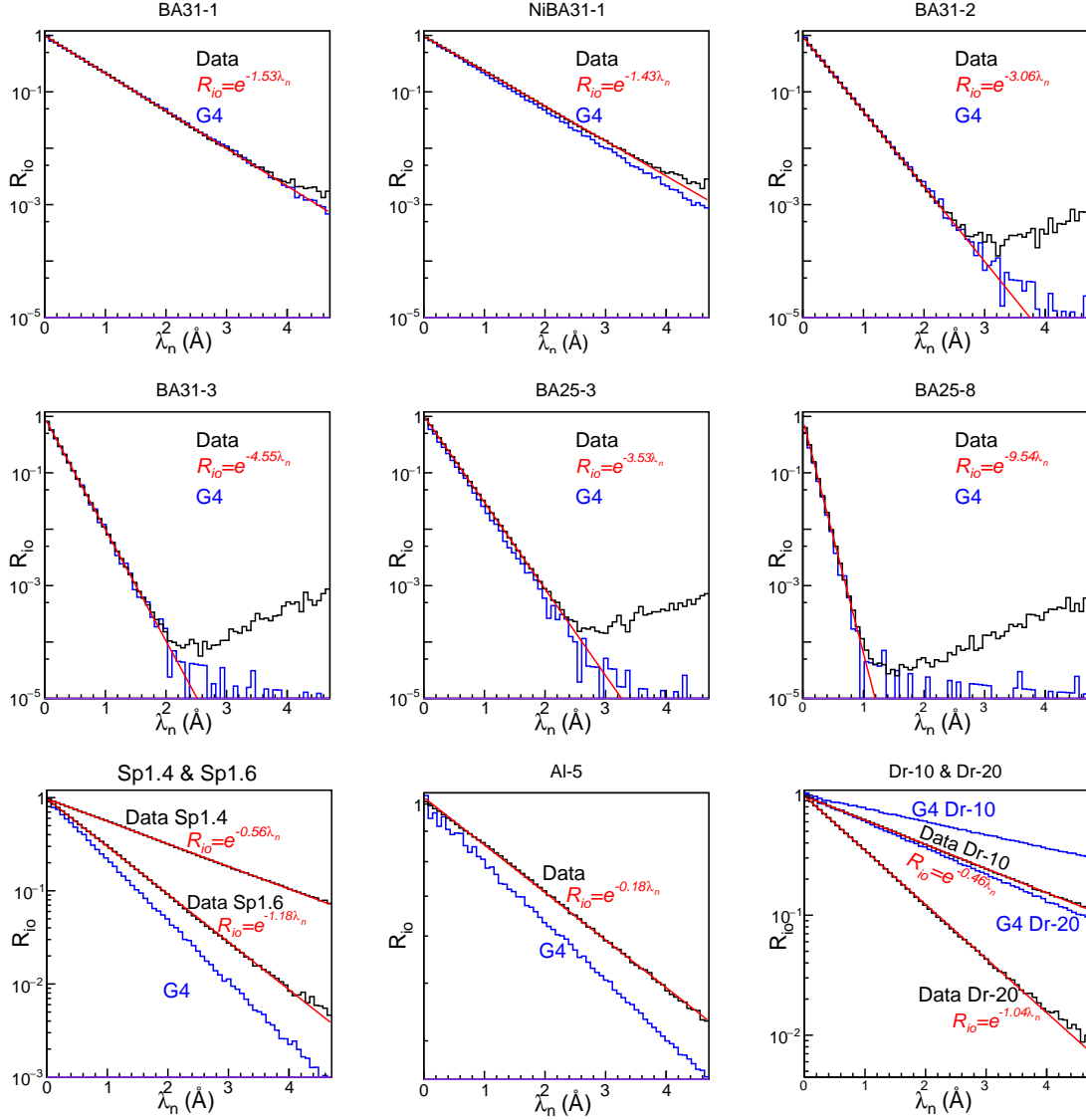


Figure 3: Average ratio R_{io} . The data are displayed in black and the red lines are exponential fits to the R_{io} data. Geant4-simulated distributions (G4) are shown in blue.

Fig. 4 displays for eight samples the probability of absorption ($1 - R_{io}$), integrated over the wavelength range $\lambda_n = 0.5\text{--}3.0\text{ \AA}$, for nGEM pixels seeing direct beam. Taking X- and Y- projections of the 2D plots gives the 1D slices shown in Fig. 5. The X-projections have been summed over Y pixels 60-64 and the Y-projections summed over X pixels 66-70.

Samples Al-5, Dr-10 and Dr-20 have slots cut for assembly into a grid, which appear in the 2D images. Al-5, Dr-10, Dr-20, Sp1.4 and Sp1.6 show variable, position-dependent absorption. Cold spray coatings (Sp1.4, Sp1.6) display a faint horizontal banded structure in $1 - R_{io}$, which is also visible to the naked eye. Al-5 sputtered coating shows relatively small variation in absorption across the face of the sheet, while dripped coatings (Dr10, Dr20) show much larger variations. Al/B₄C composite (BA31-1, NiBA31-1, BA31-3) absorption is relatively uniform across the samples.

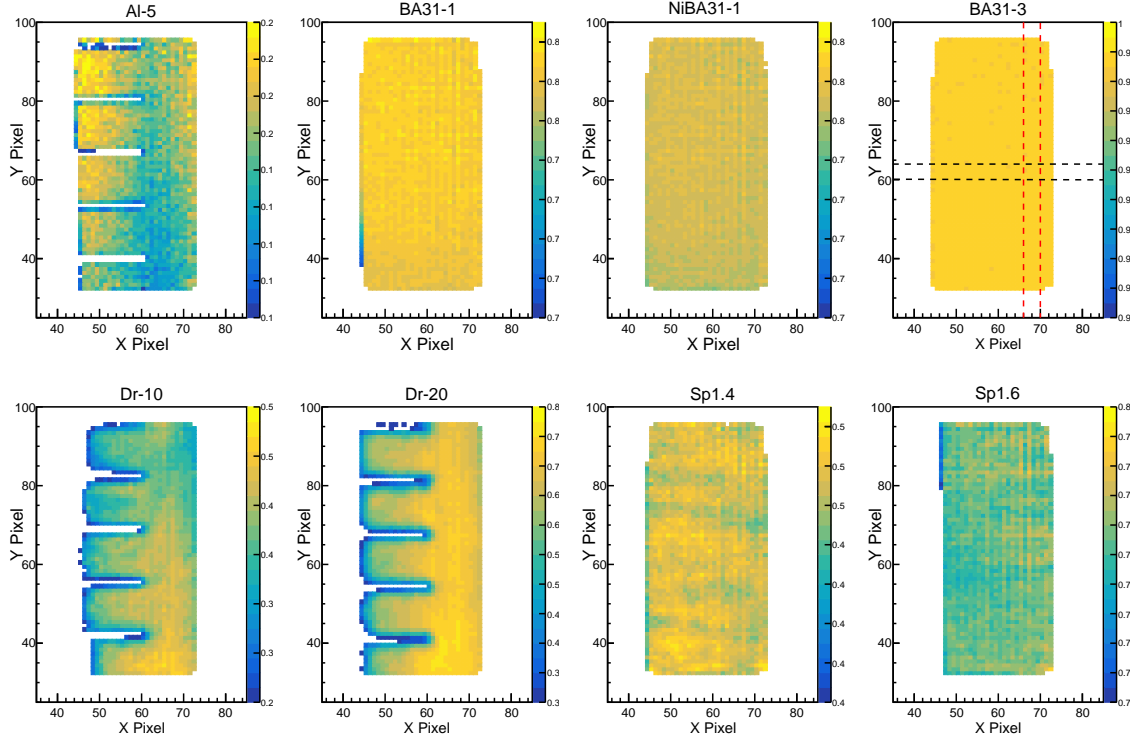


Figure 4: 2D images of neutron absorption $1 - R_{io}$ on eight samples. Note that the vertical scales of the plots are different to highlight any variations across the samples. Horizontal black dotted lines (plot BA31-3) show the limits for the X-projections in Fig. 5, while the vertical red dotted lines show the Y-projection limits.

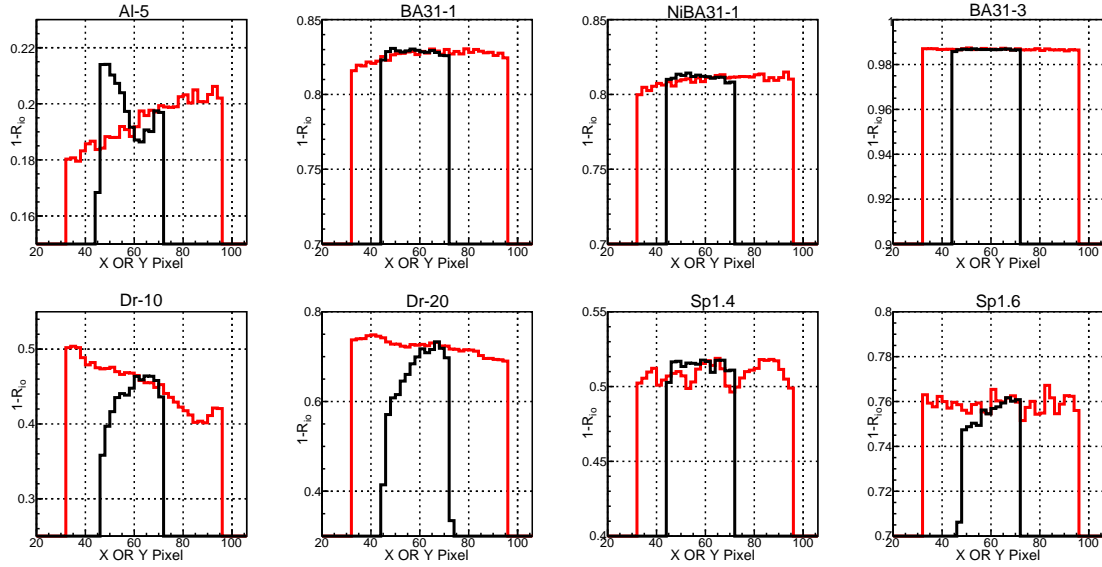


Figure 5: 1D projections of the 2D neutron absorption plots in Fig. 4, with X-projections (black) summed over y bins 60-64 and Y-projections (red) summed over x bins 66-70. Note that the Y-axis scales are different as $1 - R_{io}$ varies considerably from sample to sample.

The findings of the transmission tests are summarised as follows:

1. For the Al/B₄C composite samples the measured decay constants are close to k , so that the ¹⁰B concentration and thickness of these samples are close to the nominal values given in

Table 1. Note that the Geant4 calculation for NiBA31-1 was made for 1 mm of composite, while the actual thickness was found to be ≈ 0.95 mm. The G4 entry for NiBA31-1 in Table 1 has been scaled by a factor 0.95. From Fig. 4, 5 the mix of B₄C and Al appears quite homogeneous throughout these samples

2. The Al-5 decay constant is around 78% of k . Sputtering of B₄C powder on Al does not produce a completely uniform film of coating and it is likely that the average thickness of B₄C is ~ 4 μ m. The Al-5 plots in Fig. 4,5 show some smooth variation in $1 - R_{io}$ at the $\sim 10\%$ level.
3. Cold spray coatings of a Al/B₄C composite on Al sheet, samples Sp1.4 and Sp1.6, both show decay constants considerably smaller than k calculated for a nominal 52% B₄C content and 300 μ m coating thickness. Sp1.6 has a factor ~ 2 more ¹⁰B in the coating than Sp1.4 and both samples show a banded structure in the 2D plots of $1 - R_{io}$ (Fig. 4), but the variations in $1 - R_{io}$ (Fig. 5) are at the few percent level.
4. Dripped coatings of B₄C/epoxy mix on Al sheet give decay constants a factor ~ 2 higher than the nominal k . The nominal concentration of ¹⁰B is already 92%, so the coating thickness is likely greater than specified. The position dependence of the thickness shows substantial variation in Fig. 4, 5.

3. Neutron Scattering Measurement at Merlin

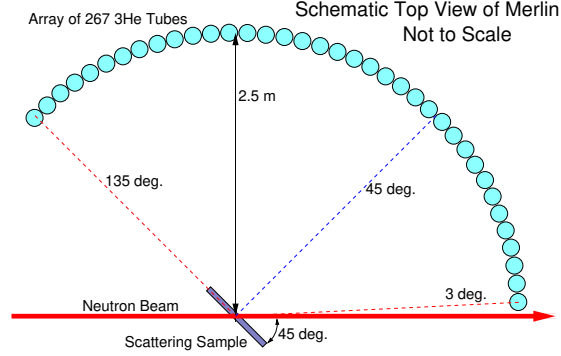


Figure 6: Simplified schematic diagram of the sample-scattering test at Merlin.

Merlin at ISIS [9] is a TOF spectrometer with medium energy resolution and a large solid angle (π sr) spanning scattering angles from 3-135° in the horizontal plane. The neutron detectors are ³He tubes 25 mm in diameter and 3 m in length, situated on an arc 2.5 m from the scattering sample.

Samples Al, Al-5, BA31-1, NiBA31-1, BA25-3 and Dr-20 were placed at the Merlin sample position, angled at 45° with respect to the beam direction, and measured for equal accumulations of proton charge at the spallation target. Measurements were made with quasi-monochromatic neutron beams at mean wavelengths of 2.41 Å (14.1 meV), 1.85 Å (24.0 meV), 1.28 Å (49.9 meV) and 0.72 Å (160 meV). Sample-out measurements were also made and subtracted from sample-in data. Fig. 7 compares 2D plots of polar scattering angle vs. energy transfer for the Al sample and sample-out background. There is considerable background at the forward angles and therefore the present analysis employed scattering angles $45^\circ \leq \theta \leq 135^\circ$.

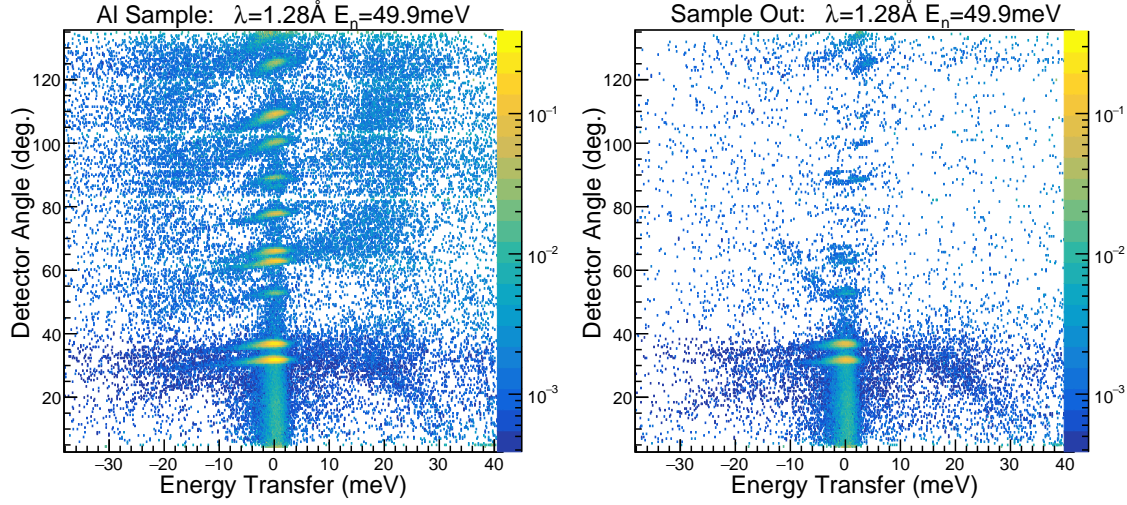


Figure 7: 2D plots of polar angle vs. energy transfer measured at Merlin. The logarithmic z scale is the same for both plots.

Fig. 8 shows the energy-transfer spectra, summed over angles $45^\circ \leq \theta \leq 135^\circ$, for the 4 beam energies and 6 scattering samples. Gaussian fits to the Al distributions produced elastic-peak widths σ . The inner red lines sitting at $\pm 3\sigma$ from zero define the elastic scattering region, while the outer red lines show shoulder regions which range from -9σ to -3σ and $+3\sigma$ to $+9\sigma$.

As Al is the main structural material of MG neutron spectrometers, the Al data have been employed as a basis with which the other samples have been compared. Thus the neutron yield scales of Fig. 8 have been normalised so that the peaks of the Al distributions sit at a value 1.0.

The ^{10}B content in samples is most effective at suppressing scattering at the longer wavelengths, where the capture cross section is highest. At 0.72 \AA BA31-1 and NiBA31-1 exhibit more scattering than Al. They contain $\sim 40\%$ more Al than the pure Al sample and there is an additional contribution to scattering from the Ni plating on NiBA31-1.

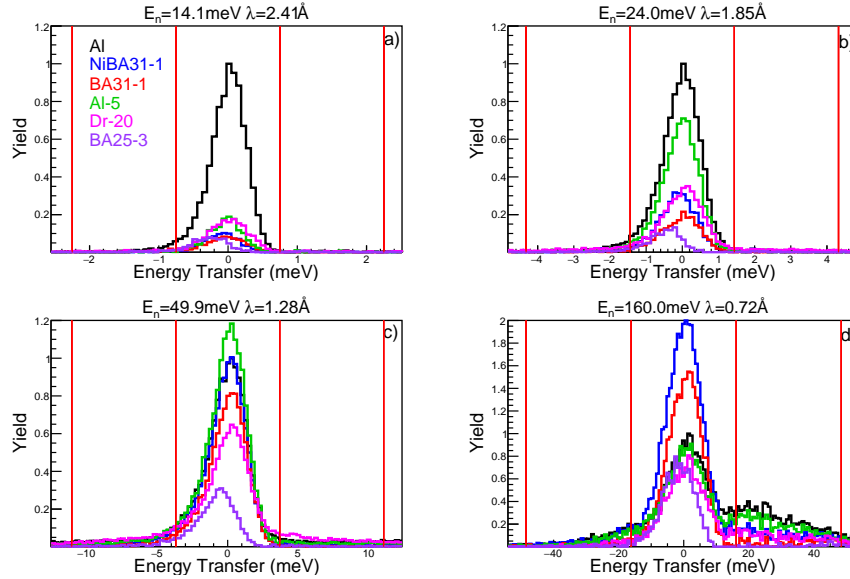


Figure 8: Energy transfer spectra summed over scattering angles $45^\circ \leq \theta \leq 135^\circ$. Sample ID is explained in Table 1. The red vertical lines denote limits for integration of the elastic peak and shoulder regions to the left and right of the peak. The width of each region is 6σ , where σ was obtained from Gaussian fits to the Al peaks at each wavelength.

The angular dependence of the scattered neutron yield, integrated over the elastic peak region, is shown in Fig. 9 (top row) for the Al, NiBA31-1 and BA31-1 samples at the four incident-energy settings. Similar to Fig. 8 the yields have been normalised so that the peak values of the Al distributions sit at 1.0.

Prominent Bragg peaks from Al scattering are suppressed in NiBA31-1 and BA31-1, although the composite samples show more incoherent scattering than pure Al at wavelengths above 2.41 Å. Comparison of NiBA31-1 and BA31-1 shows that the Ni plating increases the scattered yield slightly, but Bragg peaks from Ni are not visible.

Geant4 simulations, which implement a very simple model of the Merlin setup, are also shown in Fig. 9 (bottom row). Guided by the results of the neutron-transmission measurements (Table 1), which showed the effective thickness of ^{10}B in a sample, Merlin simulations were performed with a 4 μm B_4C coating on the Al-5 sample and a 40 μm dripped coating on the DR-20 sample. Ni thickness in NiBA31-1 was set to 20 μm , based on subsequent measurements, and 9% P (by weight) incorporated, in line with the plating supplier's specification.

The model embodies the polar and out-of-plane angular coverage of the ^3He counter array, but has no fine detail of the neutron detectors or the materials of the spectrometer in close proximity. An absolute comparison of the simulated neutron yields to the data was not possible, due to uncertainties in the data normalisation procedure. Similar to the data in Fig. 9 the simulated angular distributions have been scaled so that the peak values for Al sit at 1.0. The Geant4 model includes the NCrystal package [14], developed at ESS, to model the interaction of thermal neutrons with Al, Ni, B_4C , Al/ B_4C composite and epoxy/ B_4C dripped coating. It reproduces the general features of the Bragg-peak structure of Al and the attenuation of these peaks in the composite samples. A fully realistic model of Merlin is beyond the scope of this work and detailed differences in the angular distributions may well be due to the simple model of Merlin employed. For strongly absorbing samples the backward angle region close to 135° is sensitive to the angle of the sample with respect to the beam (nominally 45° , Fig. 6). Even a few degrees of misalignment has a sizeable effect on the backward-angle Geant4 calculation.

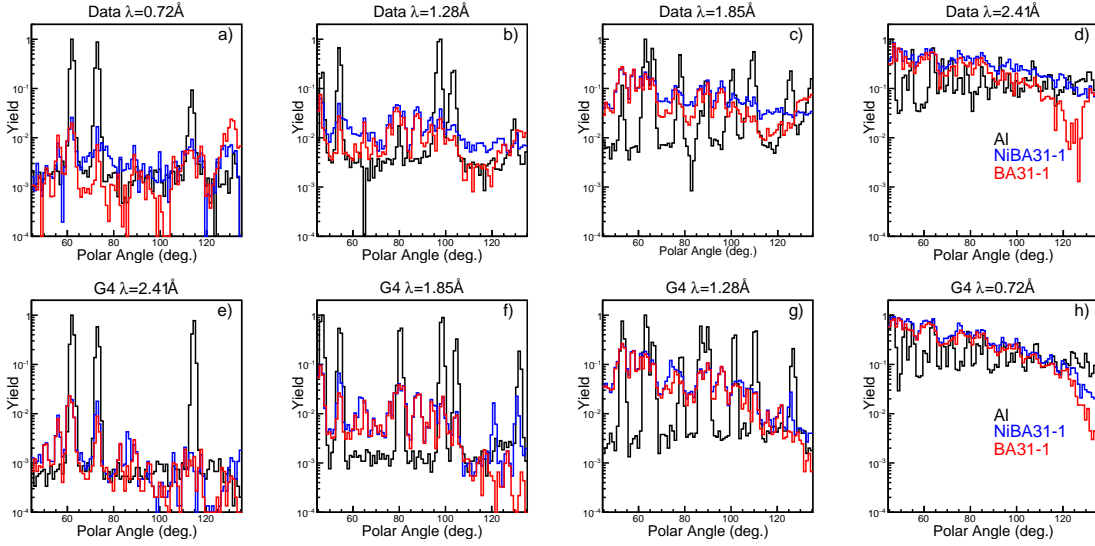


Figure 9: Scattering angle distributions for Al (black), NiBA31-1 (blue) and BA31-1 (red) samples. Top row: measurements, bottom row: Geant4 simulations. The simulated distributions have been scaled by a factor 10^{-3} to bring them on to the same range as the measurements.

The energy-transfer spectra of Fig. 8 were integrated over the elastic peak region and the shoulder regions to the left (-ve ET) and right (+ve ET) of the elastic peak. Fig. 10 compares ratios, the quotients of the sample integral and the Al-sample integral at a given λ_n . Thus the Al points sit at a value of 1.0. At longer wavelengths ($\lambda_n = 1.85, 2.41$ Å) the scattered neutron yield in the elastic region is lower, relative to Al, in samples with ^{10}B content. However at $\lambda_n = 0.72$ Å, NiBA31-1

and BA31-1 show increased scattering compared to Al. In the shoulder regions at all measured wavelengths the scattered yield is lower where the ^{10}B content is higher, apart from Dr-20, where the base material of the drip coating is epoxy resin.

As in Fig. 9, the simulation reproduces the general features of the data in the elastic-peak region. However the Merlin model, which employs a simple Gaussian TOF structure for the chopped beam, shows larger discrepancies with the data in the shoulder regions, notably for the BA31-1 and NiBA31-1 samples at $\lambda_n = 0.72 \text{ \AA}$.

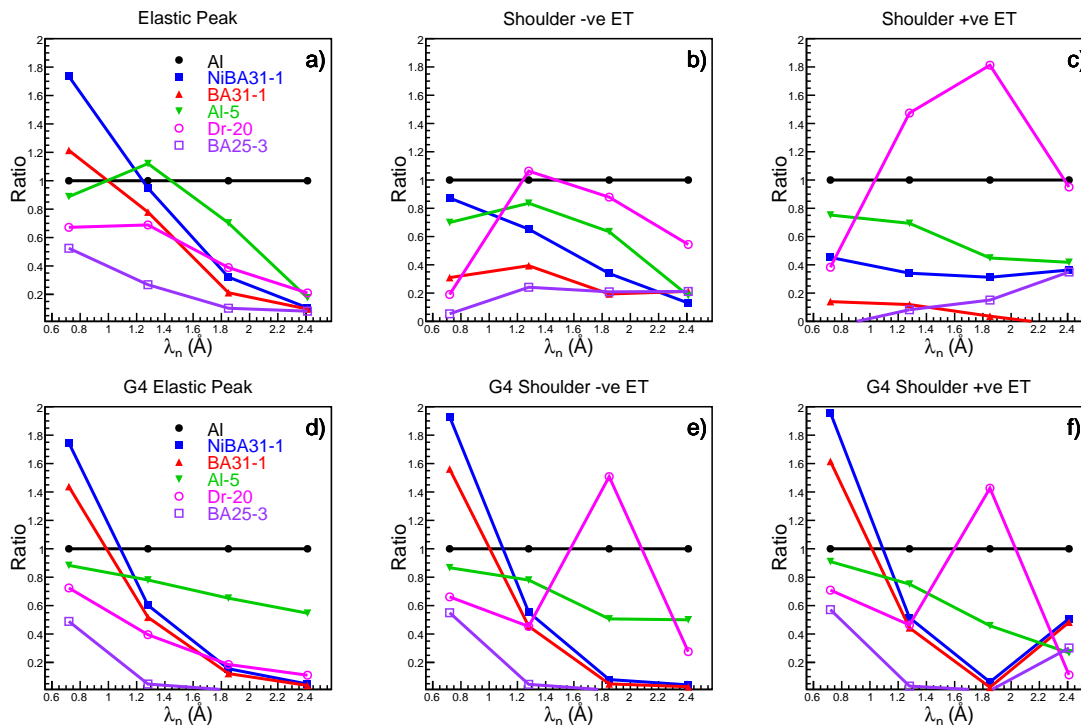


Figure 10: The dependence of scattered neutron yield ratios on scattering sample and incident neutron wavelength for the elastic and shoulder regions of the energy-transfer spectra (Fig. 8). The top row shows measured values, while the bottom row shows simulated values.

4. Conclusions and Outlook

Internal shielding is important on Multi-Grid type neutron detectors to suppress multiple scattering, which can distort measurements of energy and momentum transfer. B_4C provides effective shielding for thermal neutrons, especially if the ^{10}B content is enriched, but can be difficult to incorporate in mechanical structures.

Up to now the MG have been made from high purity Al coated with highly enriched B_4C and for the normal blades of a grid a thin sputtered coating works well. The normal-blade coating must be thin to allow the charged products of $n + ^{10}\text{B} \rightarrow ^4\text{He} + ^7\text{Li}$ to escape into the gas of the VPC. For radial blades sputtering can produce coating thickness up to $\sim 5 \mu\text{m}$ (sample Al-5) and the present measurements show significantly lower neutron transmission and scattering relative to bare Al. Monte Carlo models of T-REX suggest that use of Al-5 on the radial blades is indeed beneficial, but the benefit is increased substantially if the ^{10}B thickness on the radial blades is increased. Transmission measurements on the present sample of Al-5 show that the average coating thickness is actually $\sim 4 \mu\text{m}$. Merlin measurements show that the coating reduces the amount of neutron scattering compared to bare Al at wavelengths greater than 1.28 \AA .

Dripped coatings of a B_4C -epoxy mix (Dr-10, Dr-20) on an Al substrate have lower transmission than Al-5, although the epoxy component increases the probability of neutron scattering, especially in the non-elastic region. The present measurements suggest some difficulty to control the thickness

and uniformity of the coating. Also the long term adhesion of the coating to the Al substrate is not known.

Cold-spray coating of a B₄C/Al composite on to an Al substrate (Sp1.4 and SP1.6) also has lower transmission than Al-5, but the ¹⁰B content in the two provided samples showed large differences in the transmission measurement. The coating thickness shows a banded structure, presumably reflecting the scanning of the spray gun across the sample. Cold-spray coated samples were not available for the Merlin scattering measurement.

Overall, uncoated B₄C/Al composite samples performed best in terms of low neutron transmission and scattering. The transmission measurements show that the manufacturer’s specification of ¹⁰B content is quite accurate and the concentration appears fairly uniform throughout the volume of the sample. It is electrically conductive and can be water-jet cut and laser welded (if Ni plated). The thinnest available sheet (BA31-1) is thus suitable for radial blades. However the Al used in the composite contains traces of actinide impurities and so the sheet emits alpha particles, which are detected to produce a constant background counting rate [15]. A $\sim 25\ \mu\text{m}$ Ni plating of the composite (NiBA31-1) is highly effective at suppressing this background and adhesion of the plating to the substrate appears to be good. However the Ni coating increases neutron scattering relative to BA31-1. Of the samples tested at Merlin, BA25-3 had the lowest neutron scattering yield. Thus the thicker composite sheets, which are also highly opaque to neutrons, will be suitable for additional shielding at the rear or side of the MG structures.

Based on the measurements reported here, a Multi-Grid prototype for T-REX, named TRP-3, has been constructed using NiBA31-1 for the radial blades and BA31 (4 mm thick) for the shielding attached to the rear of the grid (Fig. 1). The latter reduces back scattering from Multi-Grid support structures. As NiBA31-1 is an effective neutron absorber no additional side shielding has been included. TRP-3 has been tested at ESS and ISIS in comparison to an earlier unshielded prototype TRP-1 and preliminary analyses show that the new internal shielding is highly effective at suppressing internal neutron scattering.

Acknowledgements

We wish to thank the following for their invaluable assistance:

- the ISIS staff for the efficient provision of the neutron beams at the EMMA and Merlin facilities,
- the technicians of the ESS Detector Group and the University of Glasgow engaged in the design and construction of Multi-Grid structures,
- Y. Yang and L. Liu of Tsinghua University, Beijing, China, who provided the drip coated sample,
- G. Zuzel and M. Czubak, of the Jagiellonian University, Kraków, Poland, who performed alpha background measurements of selected samples.

The University of Glasgow acknowledge that the result has been generated in collaboration with and through financial support by European Spallation Source ERIC under Contract 325103. Glasgow also acknowledge support from the UK Science and Technology Facilities Council, Grant ST/V00106X/1.

References

- [1] ¹⁰B *multi-grid proportional gas counters for large area thermal neutron detectors*, B. Guérard et al., Nucl. Instr. Meth. A 720, 2013, 116.
- [2] *The instrument suite of the European Spallation Source*, K.H. Andersen et al., Nucl. Instr. Meth. A 957, 2020, 163402.
- [3] *Scattered neutron background in thermal neutron detectors*, E. Dian et al., Nucl. Instr. Meth. A 902, 2018, 173.

- [4] *General considerations for effective thermal neutron shielding in detector applications*, A. Bac-kis et al. EPJ Techn. and Instrum 9, 2022, 8.
- [5] *Suppression of intrinsic neutron background in the Multi-Grid detector*, E. Dian et al., JINST 14, 2019, P01021.
- [6] *Simulation of the T-REX Multi-Grid Detector*, J.R.M. Annand, ESS/T-TREX quarterly meet-ing, 29th May 2024 <https://indico.ess.eu/event/3524/sessions/7227/attachments/15409/29163/MG.29.05.24.pdf>
- [7] *Geant4 - A Simulation Toolkit*, S. Agostinelli et al., Nucl. Instr. Meth. A 506, 2003, 250.<https://geant4.web.cern.ch/>
- [8] The EMMA test beam line at ISIS <https://www.isis.stfc.ac.uk/Pages/Instruments.aspx>
- [9] *MERLIN, a new high count rate spectrometer at ISIS*, R.I. Bewley et al., Physica B 385-386 1029-1031 (2006). <https://www.isis.stfc.ac.uk/Pages/Merlin-technical-information.aspx>
- [10] *Development of a neutron detector with a GEM*, H. Ohshita et al., Nucl. Instr. Meth. A 623, 2010, 126.
- [11] Alumeco ApS, Næsbyvej 26 5000 Odense C Denmark. mail@alumeco.dk
- [12] Impact Innovations GmbH, Germany, <https://impact-innovations.com/>.
- [13] *Total Neutron Cross Section of ^{10}B in the Thermal Neutron Energy Range*, H.W. Schmitt et al., Nucl. Phys. 17, 1960, 109.
- [14] *NCrystal: A library for thermal neutron transport*, X.-X. Cai and T. Kittelmann, Computer Physics Communications 246, 2020, 106851
- [15] *Analysis of Aluminium Samples for ESS*, G. Zuzel and M. Czubak, Jagiellonian University, Kraków, Private Communication 30th May 2025.